Galindo, J.; A. Gil; Navarro, R.; García-Olivas, G. (2022). Numerical assessment of mixing of humid air streams in three-way junctions and impact on volume condensation. Applied Thermal Engineering. 201:1-14. https://doi.org/10.1016/j.applthermaleng.2021.117676

References

[1] J. Galindo, A. Gil, R. Navarro, G. García-Olivas, Numerical assessment of mixing of humid air streams in three-way junctions and impact on volume condensation, Applied Thermal Engineering 201 (2022) 14. doi:https://doi.org/10.1016/j.applthermaleng.2021.117676.

Numerical assessment of mixing of humid air streams in three-way junctions and impact on volume condensation

J. Galindo[a], A. Gil[a], R. Navarro[a], G. García - Olivas[a,*]

[a] *CMT - Motores Térmicos, Universitat Politècnica de València*
Camino de Vera, 46022 Valencia (Spain)

Abstract

Flow mixing at three-way junctions is widely studied due to its usage in countless applications. Particularly, in air conditioning and internal combustion engines, the mixing of humid air streams can lead to volume condensation, provided that any local temperature achieves dew conditions. This work investigates and quantifies the correlation between mixing intensity and generated condensation. A method to define mixing indexes is developed, comparing its performance against literature references that employ temperature or passive scalar to evaluate mixing. A numerical campaign of 128 Reynolds-Averaged Navier Stokes three-dimensional (3D) simulations is designed to explore different junction operating conditions. A validated condensation submodel embedded in the 3D model enables the quantification of condensation at the junction outlet, which also can be estimated by means of a 0D model that provides the psychrometric state of a homogeneous mixture between the inlet streams. A strong linear correlation is found between condensation and the product of mixing indexes and 0D condensation mass flow rate, since the latter carries the psychrometric information of the working point. This connection allows to find junction design guidelines to reduce mixing and therefore condensation. Additional simulations confirm that removing junction valves, reducing mixing length, increasing the branch duct diameter and aligning the branch leg with the outlet duct significantly decrease condensation. In the framework of low pressure exhaust gas recirculation (EGR), this condensation damages the compressor wheel. If junctions are designed as suggested, the current constraints over EGR rates to limit condensation can be removed, which will result in internal combustion engines with lower emissions and better fuel consumption.

Keywords: Volume condensation, CFD, Three-way junction, Mixing index, Momentum ratio, Low-pressure Exhaust Gas Recirculation

1. Introduction and literature review

There are many engineering fields in which three-way junctions are employed to merge two flows into a single stream, such as nuclear industry [1, 2, 3], internal combustion engines [4, 5] and oil industry [6], to name a few. In

*Corresponding author. Tel.: +34 963 877 650
Email addresses: galindo@mot.upv.es (J. Galindo), angime@mot.upv.es (A. Gil), ronagar1@mot.upv.es (R. Navarro), guigarol@mot.upv.es (G. García - Olivas)

all these situations, a main stream meets a secondary flow within the junction, seeking for a quick homogenization or trying to keep the streams separated as much as possible, depending of the considered problem.

Three-way junction flow patterns have been studied by Hosseini et al. [7], Li et al. [8], and Zhou et al. [9], amongst others. Particularly, Hosseini et al. [7] established a classification regarding flow behavior in 4 categories, while Kamide et al. [10] and Kimura et al. [2] considered 3 types of flow patterns: wall-jet, deflecting-jet and impinging-jet.

The mixing process in three-way junctions has being analyzed by different researchers. Large eddy simulations have been conducted by Evrim et al. [11, 12] and Kuczaj et al. [13] in order to study thermal mixing in T-junctions. Gupta et al. [14] employed Reynolds-averaged Navier Stokes (RANS) simulations with $SST\ k-\omega$ turbulence model to find that increasing jet-to-mainstream momentum ratio enhanced mixing. However, none of these works deal with humid air streams and the condensation generated due to their mixing.

In this work, a difference is made between the terms "surface condensation" and "volume condensation". The former is driven by the presence of cooled walls (e.g., flow through a heat exchanger [15, 16]), so that related phenomena happening close to the surface (wall heat transfer and thermal boundary layer [17], existence of either dropwise or filmwise condensation [18], etc.) needs to be predicted accurately. On the other hand, volume (or bulk flow) condensation is produced when humid flow achieves dew point conditions without heat release into the surroundings, by means of gas expansion [19] or by mixing with colder flow, being the latter the object of study of this work. In this way, volume condensation may even appear when subsaturated wet streams meet. This phenomenon can become an issue in the field of air conditioning [20] and internal combustion engines [21]. In this work, the operating conditions considered correspond to junctions employed in internal combustion engines featuring Low-Pressure Exhaust Gas Recirculation (LP-EGR). This technique consists in reintroducing and mixing the exhaust gases with fresh air. By achieving a reduction of the maximum temperature in the combustion chamber, NOx emissions are abated [22, 23, 24]. LP-EGR reintroduces the exhaust gas before the compressor [25, 26], which leads to the possibility of water droplets impacting the compressor wheel if bulk flow condensation arises in the air-EGR three-way junction. LP-EGR layout provides high EGR mass flow rates [27, 28] which is deemed as one of the key factors to increase the thermal efficiency of internal combustion engines [29]. Unfortunately, the related deterioration of compressor performance and integrity [21, 30] limits the applicability of LP-EGR in the scope of cold ambients [31, 32, 33].

A 3D CFD model was developed by Serrano et al. [34] to analyze junction condensation. This model has been validated in different ways by Galindo et al. [35, 36]. Good accordance between CFD predictions and experimental results has been found in terms of secondary flows (measured by means of laser particle image velocimetry) and condensation patterns (observed with planar laser-induced visualization) [35], as well as condensation mass flow rates (indirectly obtained by temperature measurements with and without condensation) [36]. Junction design should minimize condensation mass flow rate to prevent harm to the LP-EGR compressor, as great impeller erosion was found at experimental impeller durability tests when 3D-CFD simulations predicted the highest condensation rates [37], which can be deemed as another prove of the validity of the 3D CFD model. Galindo et al. [5, 35] have observed

that junction geometries that promote strong secondary flows are the ones providing higher condensation mass flow rates, but their research did not go beyond that point. The idea that volume condensation in a three-way junction may be correlated with a quantitative indicator of the mixing of its inlet streams has never been addressed before in the literature, and is the main task of this work.

In the scope of LP-EGR, the effects of air-EGR mixing before the compressor have indeed been analyzed in the works of Brune et al. [38, 39], Vithala et al [40] and more recently by Reihani et al. [41, 42]. Particularly, the injection of EGR stream can improve the behavior of the compressor under certain conditions according to Reihani et al. [42]. However, these studies do not deal with multiphase flow, so the impact on condensation of how air is mixed with LP-EGR is assessed for the first time in the current work.

The literature review has established the potential benefits of reducing junction condensation. Despite that flow and mixing phenomena inside a three-way junction have been studied previously, there has not been (to the authors' knowledge) a work providing a quantitative correlation between mixing and condensation. The present study employs a comprehensive numerical campaign (more than 130 simulations) to provide the following original contributions in the framework of mixing and volume condensation. First, a new definition of mixing index is developed, by calculating the unmixed area at a certain section. This index can be computed by considering the transport of a passive scalar or the temperature field. The performance of these versions of the new index is compared against other mixing indexes from the literature. Second, a strong quantitative correlation is derived for the first time between condensation mass flow rate, psychrometric conditions and such mixing indexes. Third, novel junction design guidelines to decrease bulk flow condensation are obtained through the reduction of flow mixing. Particularly, the connection between branch-to-mainstream momentum ratio and mixing is originally exploited to minimize condensation.

The 0D and 3D CFD models employed in this works are described in Section 2, together with the definitions of mixing indexes and momentum ratio. Section 3 provides the correlations between condensation and mixing and the role of momentum ratio in flow patterns and mixing, as well as the design criteria that should be followed to reduce bulk flow condensation. Finally, some concluding remarks are provided in Section 4.

2. Methods

2.1. Junction 0D Model

As aforementioned, the problem studied in this work is the mixing between humid air streams in a three-way junction. Serrano et al. [21] developed a 0D model to predict the condensation mass flow rate produced in these situations by considering that both streams end up being perfectly mixed at the outlet. Figure 1 depicts the numerical domain that will be described in Section 2.2.1, but it can be used as a sketch of such 0D model to present its inputs. Considering the main (or air) leg, the mass flow ($\dot{m}_m$), pressure (P_m), temperature (T_m), and relative humidity (RH_m) must be specified. On the branch (or EGR) duct, the same conditions ($\dot{m}_b$, P_b, T_b) must be declared in exception of the relative humidity, which will be replaced by the specific humidity (w_b). In addition, the model needs the introduction

of the outlet pressure condition (P_{out}) and the 3 main areas of the domain (A_m, A_b, A_{out}). The result of the model is the condensation mass flow rate ($\dot{m}_{cond-0D}$) at the outlet of the three-way junction.

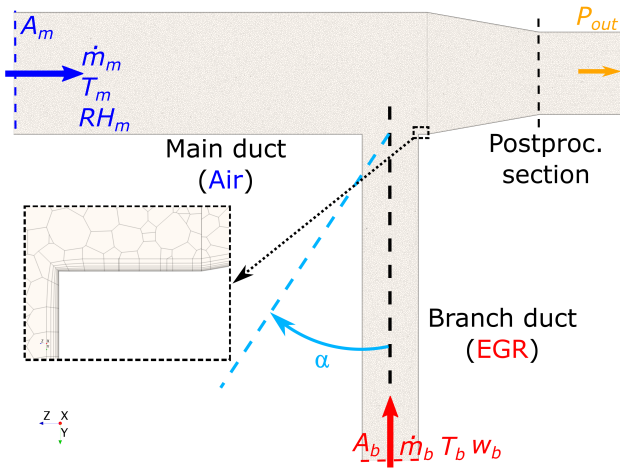

Figure 1: Longitudinal plane of T-junction numerical domain showing mesh, boundary conditions and postprocessing plane, with a close-up of the prism layer employed in the branch insertion.

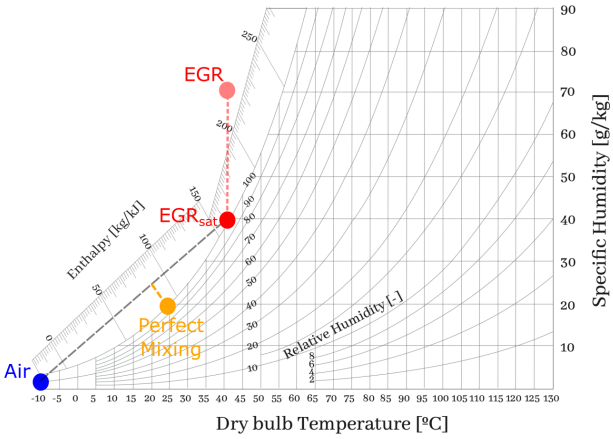

Figure 2: Psychrometric diagram at atmospheric pressure, with three-way junction inlet conditions and outlet solution obtained with 0D perfect mixing model.

Figure 2 shows a psychrometric diagram. The conditions for the inlet ducts (depicted in Fig. 1) belonging to one of the 128 working points assessed in this work are indicated in Fig. 2. The particular values of this numerical campaign correspond to the application of three-way junctions to LP-EGR, in which cold air is mixed with warm, humid EGR. Notice how the design of experiments described in Section 2.3 delivers a number of supersaturated points (as the one depicted in Fig. 2), depending on the combination of values of T_b, w_b and P_{outlet}. In such cases, the first step is to remove the excess of water at the branch duct inlet between the original point and that corresponding to saturated conditions, since both 0D and 3D CFD models (see Section 2.2) are devoted to obtain condensation only due to

mixing. The equivalent saturated point ("EGR_{sat}" in Fig. 2) is obtained by descending vertically from the original point ("EGR") up to the saturation line, since the imposed T_b is a static, dry bulb temperature.

Condensation mass flow rate is then obtained with the 0D model [21] by considering conservation of mass for air and water species, together with the definition of specific humidity w, by virtue of the following equation:

$$\dot{m}_{cond-0D} = \dot{m}_{air} \cdot \frac{w_{air}/1000}{w_{air}/1000 + 1} + \dot{m}_{EGR} \cdot \frac{w_{EGR,sat}/1000}{w_{EGR,sat}/1000 + 1} - (\dot{m}_{air} + \dot{m}_{EGR}) \cdot \frac{w_{PM}/1000}{w_{PM}/1000 + 1} \,. \tag{1}$$

In Eq. 1, the only unknown is the humidity at the outlet considering a perfect mixing between the inlet streams, i.e., w_{PM}. This solution is obtained graphically at Fig. 2 on the basis of conservation equations. First, the gray dashed line connecting the inlet points ("Air" and "EGR_{sat}") and the position at which it crosses the yellow dashed line correspond to a linear weighting of inlet specific humidities and enthalpies regarding the corresponding mass flow rates. Then, the slope of the yellow dashed line of Fig. 2 indicates constant enthalpy. This is because heat transfer with the surroundings is neglected, so that the heat released due to condensation is absorbed by the flow itself. Finally, the outlet point is located where the yellow dashed line finds the saturation line, which in turn is calculated by means of Dalton's law and Antoine's equation for humid air. The term "perfect mixing" associated to the 0D model developed by Serrano et al. [21] is here employed because the zero-dimensional consideration of the outlet station inherently assumes it to be homogeneous, and therefore the inlet streams are considered to be perfectly mixed.

This 0D model will be employed to perform correlations between condensation and mixing predicted by 3D CFD simulations (see section 3.1). Besides, section 3.2 will show that indeed the condensation predicted by this 0D model is the maximum condensation that could be achieved in the junction, when both streams are perfectly mixed. For more details about the 0D model, please refer to Serrano et al. [21].

2.2. Junction 3D CFD model

2.2.1. Geometry and mesh

Figure 1 shows a longitudinal slice of the numerical domain of the three-way junction, depicting the mesh as well. The modeled geometry represents a 90° three-way junction (T-junction) as could be featured in a LP-EGR system, where fresh air and EGR streams are mixed before the compressor. The short tapered section after the branch duct represents the compressor inlet cone, up until the postprocessing section that would correspond to the compressor inducer plane. Then, the outlet duct is extruded 5 diameters to reduce the impact of the boundary location on the region of interest.

The geometry considered in Fig. 1 is similar to those employed by Reihani et al. [42] and Galindo et al. [5, 43], since all of them include the compressor cone. Other authors [40, 44, 37] have modeled T-junctions for LP-EGR applications considering the same cross section for the outlet and main ducts. Besides, the impact of branch diameter and angle regarding the main duct on flow mixing and condensation will be assessed in Section 3.5.

The grid depicted in Figure 1 is a polyhedral mesh with prism layers to improve near wall resolution, with 3.7 million cells in total. The employed mesh density has been selected by means of an independence mesh study. The

main variable that was analyzed in this study is the condensed water $\dot{m}_{cond}$ at the end of the cone (see Fig. 1). A 10.4% of difference in condensed water is obtained when replacing a 0.4 million cells mesh by a 3.7 million cells grid. On the other hand, a finer mesh density leading to a 10.8 million cells does not significantly affects condensation compared to the 3.7 million cells grid (3.1% of difference). Having assessed the sensitivity of the mesh to a global key parameter (condensation mass flow rate), vertical profiles of passive scalar ϕ (see Section 2.2.2) at cone outlet diameter are provided in Fig. 3 to complete the analysis of discretization error. Figure 3 shows a great agreement between the profiles predicted by the grids with 10.8 and 3.7 million cells. Vertical distribution of ϕ simulated using 0.4 million cells presents significant differences with the other two at the bottom part of the cross-section (negative values of y). For the sake of limiting the computational effort, and considering that more than 130 simulations are conducted in this work (see section 2.3), the 3.7 million mesh is therefore selected for the rest of the study. In addition, this mesh provides a $y^+ < 1.5\%$ in 99% of wall cells even in the more critical conditions (higher mass flows), so this fact assures that the viscous sub-layer is always resolved.

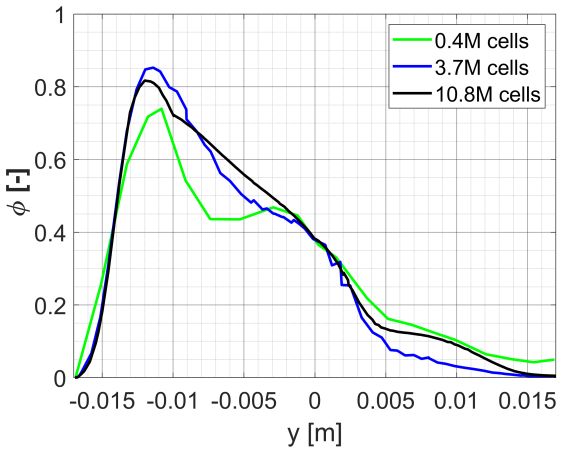

Figure 3: Profiles of passive scalar ϕ at the vertical diameter of the cone outlet for different grid resolutions.

2.2.2. *Numerical setup*

The segregated solver of STAR-CCM+ [45] has been used for the 3D CFD numerical simulations, considering second-order upwind discretization schemes for convective terms. An Eulerian approach is employed to solve the conservation equations. Since a mixture of humid air streams is aimed to be modeled, dry air and water vapor are set as ideal gas components and their corresponding species equations are included. Continuity, momentum and energy equations are also solved, which can be expressed by means of a general transport equation

$$\frac{\partial(\rho\varphi)}{\partial t} + \nabla\left(\rho\varphi u_i\right) = \nabla\left(\rho\Gamma_\varphi \nabla(\varphi)\right) + S_\varphi \,, \tag{2}$$

considering the terms of Table 1. RANS turbulence modeling will mainly affect these transport equations by boosting the *effective* diffusion coefficients of Table 1.

Table 1: Convective, diffusive and source terms for solved transport equations, excluding turbulence.

Equation	φ	Γ_φ	S_φ
Mass	1	–	S_{vap}
Species	y	D	S_{vap}
Momentum	u_i	ν	$-\partial p/\partial x_i + f_v + S_{\text{mom}}$
Energy	h_0	α	$-Dp/Dt + w_v + S_{\text{ener}}$

The condensation submodel described in Section 2.2.3 is employed to transform water vapor into liquid water when appropriate just by the implementation of custom source terms S_φ in Eq. 2, thus retaining the Eulerian approach for the sake of computational cost. In this way, features such as droplet nucleation and Lagrangian particle tracking [46, 47, 48] are not included in this model. The employed approach does not consider neither any interface tracking methods (such as Volume of Fluid) nor a fluid film model, since surface condensation is not addressed in this work.

Regarding the turbulent approach, the numerical campaign described in Section 2.3 is initially calculated using steady RANS with $SST\ k-\omega$ turbulence submodel [49]. Since the flow pattern varies significantly depending on the operating conditions (see Fig. 9), there are some working points presenting an oscillating behavior for water condensation. If the oscillation of liquid water mass flow rate at the end of the cone is above 2%, the case is switched to unsteady RANS (URANS), employing a second-order implicit transient solver. In the same way as with the mesh independence, the sensitivity to the time-step size Δt has been evaluated in terms of predicted condensation. In this way, condensation mass flow rate is modified by 0.01 % when replacing $\Delta t = 10^{-5}$ s with a larger $\Delta t = 5 \cdot 10^{-5}$ s. If the time-step size is further increased from $\Delta t = 5 \cdot 10^{-5}$ to $\Delta t = 10^{-4}$, the variation on condensed water is still slight (0.09 %). Considering again the large numerical campaign and the sensitivity analysis just performed, the unsteady cases are simulated with a time-step size of $\Delta t = 10^{-4}$ s, being in agreement with works of the same scope [37, 35].

Mass flow rate, stagnation temperature, turbulence intensity and component (dry air and water vapor) mass fraction are set at main and branch inlets. Static pressure is determined at the outlet. The particular values of boundary conditions are shown in Section 2.3. In addition, a passive scalar is injected with a value of $\phi = 1$ through the branch inlet, whereas the main inlet considers $\phi = 0$. By doing so, the mixing between the air and EGR (branch) streams can be assessed, as will be explained in Section 2.5. Walls are considered as adiabatic due to the low conductivity of a typical LP-EGR junction, which explains why volume condensation is the only mechanism in this scope.

2.2.3. Condensation submodel

In the present work, the condensation submodel was developed and verified by Serrano et al. [34]. This model is implemented in STAR-CCM+ [45], allowing to predict the amount of condensed water on a certain operating condition produced by the mixing of the humid streams along the junction.

As a summary, the condensation model compares the psychrometric state of each cell to the corresponding sat-

urated equilibrium state, in order to condense instantaneously the appropriate amount of water when supersaturation exists. To this purpose, the source terms presented in Eqs. 3, 4 and 5:

$$S_{vap} = \frac{\rho \cdot Y_{air} \cdot (w_f - w_i)}{\Delta t} \tag{3}$$

$$S_{ener} = -S_{vap} \cdot L \tag{4}$$

$$S_{mom} = S_{vap} \cdot \vec{u} \tag{5}$$

are included in the corresponding transport equations (see Eq. 2 and Table 1). The term S_{vap} is subtracted from the water vapor species and injected into a transport equation to represent the generation of condensed liquid water and its motion in the form of fog. In this way, a condensation mass flow rate can be computed at the three-way junction outlet, which will be exploited throughout Section 3. Notice also how the release of energy due to condensation (see Eq. 4) affects the temperature field, which is a feature that contributes to the inferior performance of mixing indexes defined using temperatures when compared to passive-scalar mixing indexes, as will be shown in Section 3.1. For a complete explanation of the hypotheses and characteristics of this condensation submodel, the reader is referred to the work of Serrano et al. [34].

The combination of the 3D CFD setup described in Section 2.2.2 and its embedded condensation submodel has been validated against experimental measurements regarding five different aspects. Firstly, the CFD model was able to predict secondary flows in the three-way junction outlet matching those measured with laser particle image velocimetry [35]. Secondly, planar laser-induced visualization provided experimental condensation distributions in agreement with the numerical predictions [35]. Thirdly, temperature numerical and experimental fields at the outlet cross-section were found to be similar [36]. Fourthly, condensation mass flow rates obtained by CFD simulations were in accordance with indirect experimental measurements of condensation mass flow rates [36]. Lastly, CFD predictions of condensation mass flow rate with different junction configurations were found to be strongly correlated with the impeller wear level observed in experimental durability tests [37].

2.3. Numerical campaign

An extensive numerical campaign is designed in order to explore mixing flow patterns existing at different operating conditions. Particularly, a 2^{9-2} fractional factorial design is employed, in which the impact of 9 factors on mixing and condensation is assessed through 128 simulations. The identification and assigned numerical values of factors is in accordance with the application of mixing flow in LP-EGR junctions. Nevertheless, Section 3.3 will prove that the range of flow patterns of the simulations covers the whole spectrum, so that the findings of this work are not constrained by the field of scope.

The original 2^{9-2} fractional factorial design investigates 2 levels of each factor (low and high) whereas, in this case, working points not producing any condensation were replaced by others that did, taking advantage of an additional intermediate level. Table 2 includes the different factors explored with the campaign of 128 simulations, together with the numerical values of the 2 or 3 levels assessed (where appropriate):

Table 2: Factors and levels of conducted numerical campaign.

Factor	Definition	Low	Mid	High
$\dot{m}_m$ $[kg/s]$	Mass flow rate of main duct	0.014	-	0.083
EGR_{rate} $[\%]$	EGR rate (see Eq. 6)	10	25	40
T_m $[K]$	Static temperature of main duct	263	-	283
T_b $[K]$	Static temperature of branch duct	314	324	334
RH_m $[\%]$	Relative humidity of main duct	50	-	100
w_b $[g/kg]$	Specific humidity of branch duct	30	50	70
I_m $[\%]$	Turbulence intensity of main duct	1	-	10
I_b $[\%]$	Turbulence intensity of branch duct	1	-	10
P_{outlet} $[kPa]$	Outlet static pressure	80	90	100

The factors analyzed in this work (see Table 2) can be classified into different categories. On the one hand, P, T_m, RH_m are ambient variables which are independent from the engine operating conditions. On the other hand $\dot{m}_m$, EGR_{rate}, T_b and w_b are determined by the working point of the engine. Notice that in this work the branch (EGR) mass flow rate is indirectly established by the value of the engine EGR rate (EGR_{rate}), which is defined as follows:

$$EGR_{rate} = \frac{\dot{m}_{EGR}}{\dot{m}_{EGR} + \dot{m}_{air}} = \frac{\dot{m}_b}{\dot{m}_b + \dot{m}_m} \tag{6}$$

Besides, variables w_b and RH_m are directly related with the boundary conditions Y_{air} and Y_{vap} described in section 2.2.2, that are required by the simulations. In addition, the impact of turbulence intensity at the air and EGR inlet boundaries is also evaluated through this design of experiments.

The set of works conducted by Galindo et al. [35, 36, 37] to validate the 3D CFD condensation model employed operating conditions in the following range: $\dot{m}_m \in [0.024, 0.067]\, kg/s$, $EGR_{rate} \in [15, 32]\, \%$, $T_m \in [263, 273]\, K$, $T_b \in [323, 363]\, K$ and $w_b \in [50, 70]\, g/kg$. Therefore, the validation extends over most of the range of the numerical campaign described by Table 2.

2.4. Definition of momentum ratio (J) and review of literature values

The literature review conducted in the introduction (see Section 1) has shown that some authors [10, 2] claim that the ratio between the momentum of branch and main streams dictates the type of flow pattern, provided that the

junction design is kept. Momentum ratio (J) is therefore defined as:

$$J = \frac{\rho_b \cdot U_b^2}{\rho_m \cdot U_m^2}, \tag{7}$$

where ρ_b and U_b are the density and velocity in the branch respectively and ρ_m and U_m the density and the velocity in the main duct.

This parameter J is employed whenever a jet is transversely discharged from a duct into a cross-stream, that can be also confined (three-way junction) or not (jet in crossflow [50, 51]). This work deals with the former, so that the existence of an internal flow can be used to evaluate the momentum ratio of Eq. 7 in terms of the boundary conditions of the problem. Besides, in the analyzed three-way junctions, the branch duct may not be perpendicular to the main duct (see Fig. 1). In order to employ a normal branch-to-main momentum ratio, the following definition will be considered hereinafter:

$$J = \frac{\dot{m}_b^2 \cdot \rho_m \cdot A_m^2}{\dot{m}_m^2 \cdot \rho_b \cdot A_b^2} \cdot cos(\alpha)\,, \tag{8}$$

which can be expressed in the following form when combined with Eq. 6:

$$J = \frac{{EGR_{rate}}^2 \cdot \rho_m \cdot A_m^2}{(1 - EGR_{rate})^2 \cdot \rho_b \cdot A_b^2} \cdot cos(\alpha)\,. \tag{9}$$

In Eqs. 8 and 9, α is the insertion angle of the branch duct as defined in Fig. 1. $\alpha = 0°$ corresponds to a perpendicular branch duct (T-junction) and positive values of α decrease the normal branch-to-main momentum ratio J, as will be explored in Section 3.5.

2.5. Reference definitions and new proposals for mixing indexes (MI)

As mentioned in Section 1, this work studies the mixing process between two humid air streams at a three-way junction (see Fig. 1), with the goal of assessing the impact of such mixing in the generated condensation. To do so, it is required to use indicators that allow to quantify how well or bad mixed is the analyzed flow at a certain cross-section of the junction.

2.5.1. Mixing indexes on the basis of passive scalar ϕ

Calculating the transport of a passive scalar is a common technique to trace mixing in junctions [44, 52, 53]. It consists in considering a scalar that is advected by the flow without having any impact on the flow field itself, therefore behaving as a postprocessing tool. Section 2.2.2 explained that the branch leg considers a value of $\phi = 1$ and the main leg presents $\phi = 0$. In this way, the value of the passive scalar employed in this work plays the role of a branch (EGR) mass fraction, which can be understood as a local EGR_{rate} (see Eq. 6).

Researchers in the scope of flow mixing [54, 55, 56] often rely on such concentration quantities to define coefficients based on squared concentration deviations, in the spirit of the *intensity of segregation* developed by Danckwerts

[57]. A discrete version of Danckwerts' mixing index (MI) is considered in this work as a reference for mixing assessed by a passive scalar, with the following definition:

$$MI_{\phi-ref} = 1 - \frac{1/N \cdot \sum (\phi_i - \bar{\phi})^2}{\bar{\phi}\,(1-\bar{\phi})} \tag{10}$$

In Eq. 10, N is the total amount of elements of the analyzed section, ϕ is the mass fraction of the passive scalar and i is the index of each cell face at the postprocessing cross-section. Application of Eq. 10 to both inlet ducts provides an indeterminate form of type 0/0. On the one hand, the main duct presents pure air, so for each cell $\phi_i = 0$ and therefore $\bar{\phi} = 0$. On the other hand, the branch duct presents pure EGR, so $\phi_i = 1$ and $\bar{\phi} = 1$. Once the streams meet and $\bar{\phi} \neq \{0, 1\}$, Eq. 10 requires $\phi_i = \bar{\phi}$ at each and every cell of the cross section to consider that the streams are perfectly mixed ($MI_{\phi-ref} = 1$). If the flow is instead totally segregated, i.e., some cells present $\phi_i = 1$ whereas the rest of elements present $\phi_i = 0$ (there are no cells with an intermediate value of ϕ_i), then $MI_{\phi-ref} = 0$. [1]

In the present work, the definition of a new mixing index $MI_{\phi-new}$ employing the passive scalar ϕ has been developed, which will be obtained as:

$$MI_{\phi-new} = 1 - \frac{\sum_i dA_{unmixed-\phi,i}}{\sum_i dA_i}\,. \tag{11}$$

The underlying idea of the proposed index $MI_{\phi-new}$ is to quantify the unmixed area in a cross-section. To do so, a piecewise definition is considered for each surface element of the analyzed section:

$$dA_{unmixed-\phi,i} = \begin{cases} \dfrac{\phi_i - \bar{\phi}}{(1-\bar{\phi}) + \delta_{\phi-new}} \cdot A_i & \text{if} \quad \bar{\phi} \leq \phi_i \leq 1 \\ \dfrac{|\phi_i - \bar{\phi}|}{|0-\bar{\phi}| + \delta_{\phi-new}} \cdot A_i & \text{if} \quad 0 \leq \phi_i \leq \bar{\phi} \end{cases} \tag{12}$$

where $\bar{\phi}$ is the average of the passive scalar in the section. In this way, Eq. 12 classifies the element as rich (top) or lean (bottom) in terms of branch passive scalar ϕ. Then, it weights the element area linearly between a local mixture that coincides with the corresponding section average (which adds zero element area to the unmixed surface) and a fluid parcel coming purely from the main or branch inlet (which keeps its whole element area). Notice that numbers "1" and "0" appearing at the denominators of Eq. 12 correspond to the value of passive scalar at branch and main legs, respectively, and $\delta_{\phi-new}$ is a small quantity that has a negligible impact in the results but avoids division by zero. Hence, the developed mixing index $MI_{\phi-new}$ behaves like $MI_{\phi-ref}$ in the asymptotic cases, i.e., it provides $MI_{\phi-new} = 0$ for a completely segregated outlet stream and yields $MI_{\phi-new} = 1$ only for a homogeneous mixture. Besides, the proposed index avoids the indetermination of $MI_{\phi-ref}$ at the inlet legs, as it presents a value of $MI_{\phi-new} = 0$ at the main and branch ducts

[1] Considering Z elements with a value of $\phi_i = 1$ and $N-Z$ elements presenting $\phi_i = 0$, Eq. 10 results in $MI_{\phi-ref} = 1 - \frac{1/N\left[Z(1-Z/N)^2 + (N-Z)(0-Z/N)^2\right]}{Z/N(1-Z/N)}$, which yields $MI_{\phi-ref} = 0$.

Sakowitz et al. [44] also defined a *uniformity index* ranging from 0 to 1 that bears a resemblance to the combination of Eqs. 11 and 12. However, they employed a reference value corresponding to maximum heterogeneity to normalize their index, instead of the piecewise definition of Eq. 12.

2.5.2. *Mixing indexes on the basis of temperature*

An incompressible flow with adiabatic walls presents a temperature flow field that behaves exactly as a passive scalar. This fact can be exploited by experiments to compensate for the impossibility of considering a virtual passive scalar. Temperature is even employed by mildly compressible flows as an indicator of the existence and intensity of compressor stall [58, 59, 60]. In this work the ideal gas equation is considered for humid air, but local mach number M at the T-junction does not exceed a value of $M = 0.55$ for the whole numerical campaign described in Section 2.3.

A non-dimensional temperature field normalized with the difference between main and branch inlet temperature could be employed for analyzing mixing [13, 61]. However, this method assigns the ends of the [0–1] range to each of the inlet legs, whereas the perfect mixture lays in an intermediate point. For the sake of a fair comparison with the mixing indexes defined in Section 2.5, the work of Brune et al. [38] is considered instead. Brune et al. calculate a perfectly-mixed adiabatic temperature T_{ad} as:

$$T_{ad} = \frac{\dot{m}_m \cdot T_m + \dot{m}_b \cdot T_b}{\dot{m}_m + \dot{m}_b} \,. \tag{13}$$

After that, they define a local mixing rate ϵ_i, depending on the cell temperature and hot and cold temperatures of the problem, which are T_b and T_m in this case. The definition of the local mixing rate is presented in equation 14:

$$\epsilon_i = \begin{cases} \dfrac{T_i - T_b}{T_{ad} - T_b} & \text{if} \quad T_{ad} < T_i < T_b \\ \dfrac{T_i - T_m}{T_{ad} - T_m} & \text{if} \quad T_m < T_i < T_{ad} \end{cases} \tag{14}$$

with T_i being the temperature of each element i of the considered cross-section. Finally, the overall mixing index MI_{T-ref} is computed as:

$$MI_{T-ref} = \epsilon = \frac{1}{N} \sum_{i=1}^{N} \epsilon_i, \tag{15}$$

which will be considered in this work as the reference mixing index on the basis of temperature (virtual) measurements. The method of Brune et al. [38] as defined by Eqs. 13 to 15 aims at obtaining values of $MI_{T-ref} = 0$ for unmixed flow and $MI_{T-ref} = 1$ for a perfect mixture, like $MI_{\phi-ref}$ and $MI_{\phi-new}$. Indeed, this is true for a non-reactive and incompressible flow of dry air. However, in this problem the released heat due to condensation (see Eq. 4) changes the perfect-mixing temperature from that considered with the inlet temperatures alone (Eq. 13). Besides, this adiabatic temperature does not take into account that in an unsteady simulation the mass flow rates of main and branch streams arriving at a section are not necessarily those defined at the boundaries for each and every time step.

To overcome these issues, Eq. 12 is adapted to use temperature instead of a passive scalar to provide the following equation:

$$dA_{unmixed-T,i} = \begin{cases} \dfrac{T_i - \bar{T}}{(T_b - \bar{T}) + \delta_{T-new}} \cdot A_i & \text{if} \quad \bar{T} \leq T_i \leq T_b \\ \dfrac{|T_i - \bar{T}|}{|T_m - \bar{T}| + \delta_{T-new}} \cdot A_i & \text{if} \quad T_m \leq T_i \leq \bar{T} \end{cases} \tag{16}$$

in which $\bar{T}$ is the average temperature at the considered cross-section and time step. Finally, the proposed mixing index based on temperature (MI_{T-new}) is calculated as:

$$MI_{T-new} = 1 - \frac{\sum_i dA_{unmixed-T,i}}{\sum_i dA_i} \, . \tag{17}$$

3. Results and discussion

3.1. Correlation between condensation and mixing

The main hypothesis of this work is the idea that bulk flow condensation can be explained by two independent factors: psychrometry and mixing. The 0D model presented in Section 2.1 provides the maximum amount of condensation $\dot{m}_{cond-0D}$ for a certain working point considering that the streams are perfectly mixed, thus carrying the psychrometric information. If the mixing indexes MI defined in Section 2.5 are interpreted as the ratio between actual and maximum (perfect) mixture, the real condensation mass flow rate for a three-way junction at certain operating conditions could be predicted by Eq. 18:

$$\dot{m}_{cond-pred} = \dot{m}_{cond-0D} \cdot MI \, . \tag{18}$$

Equation 18 allows a comparison between the predicted condensation $\dot{m}_{cond-pred}$ and the real condensation mass flow rate $\dot{m}_{cond-obs}$ as obtained from 3D CFD (see Section 2.2) at the junction postprocessing section for the whole numerical campaign consisting in 128 simulations. At each working point, $\dot{m}_{cond-0D}$ is calculated from the boundary conditions whereas the different mixing indexes MI defined in Section 2.5 are computed at the target section, to assess the potential of each MI in terms of fitting ability.

Figure 4 depicts the comparison between condensation mass flow rate observed $\dot{m}_{cond-obs}$ (calculated by means of the 3D CFD model) and $\dot{m}_{cond-pred}$ predicted by Eq. 18, using mixing indexes based on passive scalar (Eqs. 10 and 11). Figure 5 is the counterpart of Fig. 4 for mixing indexes based on temperature (Eqs. 15 and 17). As discussed in Section 2.2.3, the CFD model provides mass flow rate $\dot{m}_{cond-obs}$ by simulating volume condensation due to the mixing of humid streams.

Bisector of Fig. 4 indicates the ideal situation in which $\dot{m}_{cond-pred} = \dot{m}_{cond-obs}$. However, Fig. 4 shows how the set of points calculated with Eq. 18 by means of $MI_{\phi-new}$ and $MI_{\phi-ref}$ consistently underpredict condensation, which also happens if MI_{T-new} and MI_{T-ref} are employed instead (see Fig. 5). Examining Eq. 18, several factors can be blamed

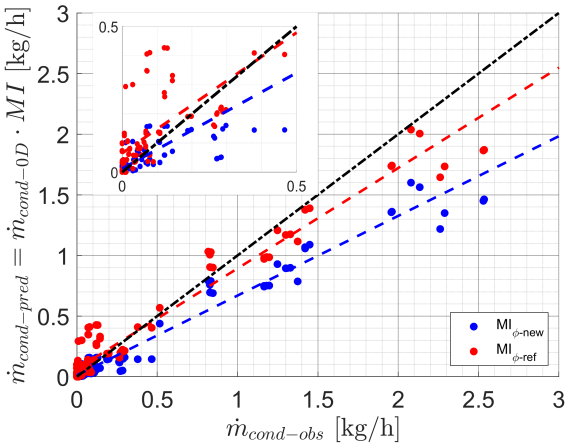

Figure 4: Calibration plot of observed versus predicted condensation (obtained using two mixing indexes based on passive scalar), with close-up of the range of $\dot{m}_{cond} = 0 - 0.5\ kg/s$. Bisector and regression lines are also included.

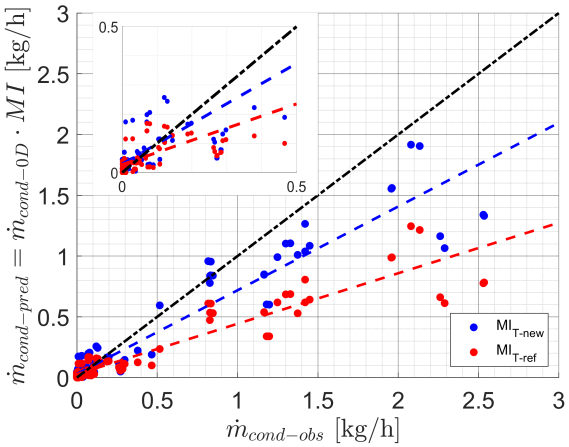

Figure 5: Calibration plot of observed versus predicted condensation (obtained using two mixing indexes based on temperature), with close-up of the range of $\dot{m}_{cond} = 0 - 0.5\ kg/s$. Bisector and regression lines are also included.

for the underprediction of condensation using that expression. Firstly, mixing indexes defined in Section 2.5 are used in Eq. 18 to predict the ratio between the actual condensation and the maximum one, according to global psychrometric considerations. Considering the non-linear behavior of psychrometry (see Section 2.1), modifications to the definition of the mixing could enhance their ability to predict $\dot{m}_{cond}$ using Eq. 18. For instance, the linear weighting between total segregation and homogeneous flow employed in $MI_{\phi-new}$ (Eq. 12) and MI_{T-new} (Eq. 16) could be replaced by other weightings that perform better for different junctions and operating conditions. Secondly, Section 3.2 will show that maximum condensation is achieved sooner than perfect mixing. Eq. 18 attributes all three-dimensional effects to MI, calculating $\dot{m}_{cond-0D}$ with the inlet psychrometric conditions and the junction inlet and oulter cross-sections (see Section 2.1). However, local low temperatures due to formation of *vena contracta* and subsequent flow expansion

may achieve dew conditions before expected and thus be responsible for a fraction of the observed underprediction of condensation.

Mean absolute error MAE is calculated for the whole numerical campaign as follows:

$$MAE = \frac{1}{K} \cdot \sum_{k=1}^{K=128} \left| \dot{m}_{cond-obs,k} - \dot{m}_{cond-pred,k} \right| . \tag{19}$$

MAE is employed in table 3 to assess the performance of the different mixing indexes studied in this work in terms of their *a priori* predicting capability of $\dot{m}_{cond}$ using Eq. 18. Table 3 shows that $MI_{\phi-ref}$ presents the lowest MAE. Notice that Fig. 4 illustrates that the cloud of red points ($MI_{\phi-ref}$) are not so far from the bisector, which would indicate perfect agreement between $\dot{m}_{cond-pred}$ and $\dot{m}_{cond-obs}$. Indeed, the regression line of $MI_{\phi-ref}$ is closer to the bisector than the regression line corresponding to $MI_{\phi-new}$, which is in agreement with the MAE values featured in table 3. Likewise, the important difference of slope between the bisector and the regression line of MI_{T-ref} in Fig. 5 is related to the largest MAE in table 3, which is presented by the same index (MI_{T-ref}).

Table 3: Mean absolute error (MAE) of observed vs predicted condensation using different mixing indexes.

Mixing index	MAE $[kg/h]$
$MI_{\phi-new}$	0.12
$MI_{\phi-ref}$	0.09
MI_{T-new}	0.11
MI_{T-ref}	0.19

Even though Eq. 18 considering the mixing indexes of Section 2.5 is not suitable to predict $\dot{m}_{cond}$ *a priori*, the linear regression lines depicted in Fig. 4 show interesting features. The coefficient of determination R^2 can be computed for the corresponding regressions as:

$$R^2 = 1 - \frac{\sum_{k=1}^{K=128} (\widehat{\dot{m}_{cond-pred,k}} - \dot{m}_{cond-pred,k})^2}{\sum_{k=1}^{K=128} (\dot{m}_{cond-pred,k} - \overline{\dot{m}_{cond-pred}})^2} . \tag{20}$$

Table 4 proves that linear regressions provide an excellent fit for the pairs $\left(\dot{m}_{cond-pred}, \dot{m}_{cond-obs}\right)$, as suggested by Fig. 4. Therefore, a calibrated line could be used to predict *a posteriori* $\dot{m}_{cond}$ by calculating the corresponding MI and employing Eq. 18. Equation 18 also proves that $\dot{m}_{cond-obs}$ is strongly and positively correlated with the mixing indexes. In this way, reducing MI should entail a decrease in condensation, which will be confirmed by sections 3.2 and 3.5.

3.2. Longitudinal evolution of mixing and condensation and effect of valves

In Section 3.1, it has been shown that condensation depends on psychrometric boundary conditions and mixing. In this section, a single working point is considered, seeking for factors that affect mixing (and hence condensation)

Table 4: Coefficient of determination (R^2) for linear regressions of condensation predicted using different mixing indexes.

Mixing index	R^2
$MI_{\phi-new}$	0.96
$MI_{\phi-ref}$	0.95
MI_{T-new}	0.90
MI_{T-ref}	0.87

regardless of the operating conditions. The point selected from the numerical campaign (see section 2.3) is the one depicted in the psychrometric diagram of Fig. 2.

Two elements are found to produce a significant impact on mixing and condensation: three-way junction geometry and mixing length. Concerning the former, it is important to remind that the objective of this work is to find universal design guidelines in a methodical and justified way, so optimization algorithms will not be employed just for the sake of providing the best geometry for this particular case. Section 3.5 will explore how to reduce mixing and condensation through the decrease of momentum ratio J, whereas in this section the effect of including junction valves is assessed.

In the scope of LP-EGR, at least one valve is required in the EGR line to obtain the desired EGR rate [62, 63]. If the obtained EGR rate is below the target even with the EGR valve wide open, there are several choices to increase it: a blower can be employed in the EGR line [64], an exhaust flap can be introduced to generate backpressure [65] or a valve can throttle the intake stream before the branch line [66]. The latter is often preferred by automotive manufacturers due to the lower cost [67], creating a compact two-valve junction [34, 37, 5]. An example of such a two-valve three-way junction (bottom part of Figure 6) is compared in this section against the standard case without valves (top part of Figure 6). The dual-valve geometry presents valves whose diameter agrees with the corresponding duct, which are opened 45° and located 1 corresponding diameter (main duct) and 2 corresponding diameters (branch duct) upstream the intersection of pipes.

In Figure 6 the line integral convolution (LIC) of velocity is combined with contours of turbulent viscosity ratio for both cases. In addition, tangential velocity vectors have been added to the representation. All these variables have been time-averaged.

In the standard, valveless case (top part of Fig. 6) the branch stream penetrates deeply in the main duct, forcing the inlet stream to surround it and fill the lower side of the cone, creating secondary flows that increase mixing in this region. When valves are implemented in the junction (bottom part of Fig. 6), both mechanisms of convective mixing are enhanced. Increase of turbulent viscosity ratio due to the valves as depicted in Fig. 6 results in a greater effective diffusion, whereas the secondary flows created due to detachment at the valves promote an increase of vorticity (not shown here) which boosts the advective mixing.

Figure 7 plots the longitudinal evolution of $MI_{\phi-new}$ (defined in Eq. 11) along the main duct for the valveless and dual-valve junctions. The evolution is obtained by sampling the main duct with a set of cross-sections and then

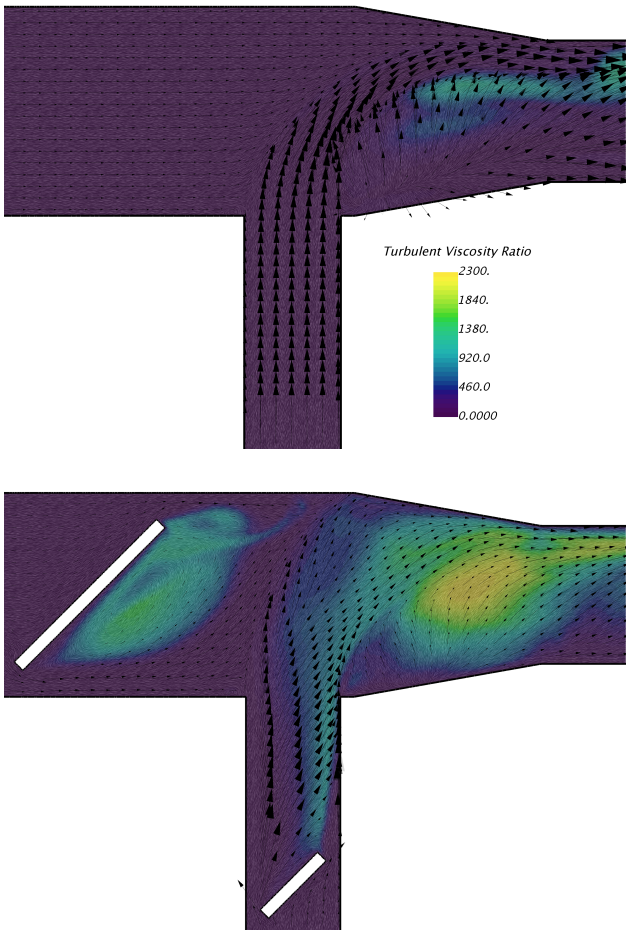

Figure 6: Time-averaged results of tangential velocity vectors superimposed over LIC of velocity combined with turbulent viscosity ration contours, for valveless case (top) and dual-valve junction (bottom).

conducting the area and time average of $MI_{\phi-new}$ for each surface.

Figure 7 starts in the ducts intersection and shows a monotonously increasing mixing index for both cases. As described in Section 2.2.1, distance between the end of the cone and the outlet boundary is 5 diameters, so these cases would require a greater length to further develop the mixing and eventually reach homogeneous flow ($MI_{\phi-new} = 1$). In any case, dual-valve junction $MI_{\phi-new}$ is greater than the corresponding value of the valveless case at the same location. Therefore, the change of flow features shown in Fig. 6 indeed improve mixing according to Fig. 7.

Figure 8 compares the axial evolution of generated condensation for the same junction geometry with and without valves. Again, condensation mass flow rate through each cross-section is averaged over time.

Figure 8 presents a similar behavior for condensation than the one observed for $MI_{\phi-new}$ (depicted in Fig. 7), which proves again the connection between mixing and condensation. In this case, Fig.8 shows that condensation grows with increasing distance to the pipe intersection and the dual-valve junction provides more condensation than

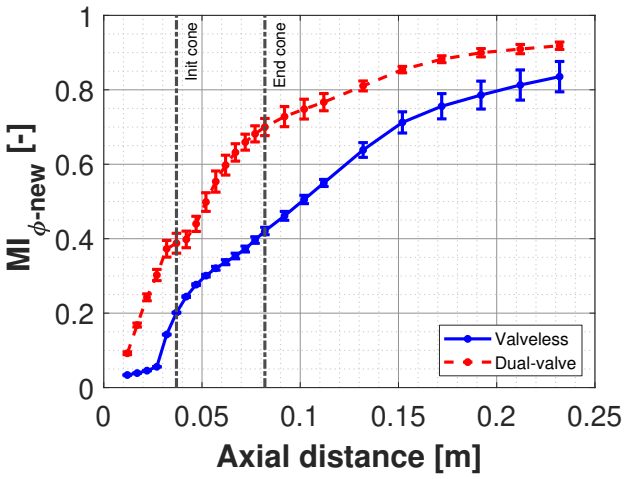

Figure 7: Longitudinal evolution of time-averaged $MI_{\phi-new}$ along the main duct for the valveless and dual-valve junctions, with vertical bars representing one standard deviation regarding transient fluctuations.

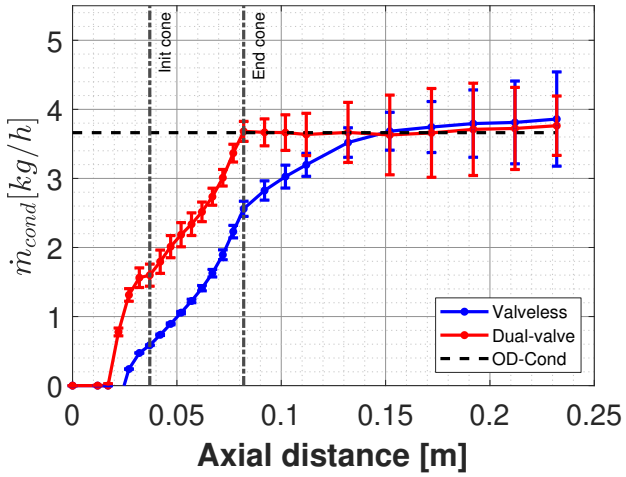

Figure 8: Longitudinal evolution of time-averaged condensation mass flow rate along the main duct for the valveless and dual-valve junctions, with vertical bars representing one standard deviation regarding transient fluctuations and $\dot{m}_{cond-0D}$ being indicated by a horizontal dashed line.

the valveless geometry. The unsteady oscillations in condensation mass flow rate represented by the vertical bars of Fig. 8 start being noticeable before the cone inlet for the dual-valve geometry whereas, for the valveless junction, these fluctuations are not significant until the last section of the tapered duct. The different behavior is in agreement with the features of vorticity and turbulent viscosity ratio already described for Fig. 6, with the branch jet creating flow disturbances even at the beginning of the cone region. The interface streams in three-way junctions is known to present transient oscillations and eddies that enhance mixing [68], and this phenomenon requires a different length to develop depending on the flow pattern.

The main difference between mixing and condensation longitudinal evolution is that the asymptotic trend to the

theoretical upper bound of condensation ($\dot{m}_{cond-0D}$ as calculated by the 0D perfect mixing model described in Section 2.1) is achieved sooner in Fig.8 than the value of 1 (perfect mixing) in Fig. 7. This can be explained by the underprediction of condensation mass flow rate of Eq. 18 discussed in Section 3.1.

3.3. Mixing flow patterns

Sections 3.1 and 3.2 have proved that there is a strong correlation between condensation and mixing. This section performs a qualitative analysis of the mixing flow patterns and compares at these situations the scalar fields that can be employed to evaluate mixing (temperature and passive scalar ϕ) and the mass fraction of condensed water Y_{H_2O-liq}.

This work follows the classification conducted by Kamide et al. [10] and Kimura et al. [2], which identified 3 types of flow patterns: wall-jet, deflecting-jet and impinging-jet. According to Kamide et al. and Kimura et al., these flow modes are determined by the ratio of branch and main stream momentum, which can be evaluated with the parameter J defined in Eq. 8. Table 5 shows the values of momentum ratio J in the different studies conducted in this work, compared to other works existing in the literature.

Table 5: Literature review of assessed range of values for momentum ratio J.

Work (Sections)		Scope	Fluid	A_m/A_b	α [°]	J [-]
Current work	(3.1, 3.4)	EGR	Gas	5	0	0.3–14
	(3.5)			5	0–60	5.7–11.4
	(3.5)			5–1.25	0	0.7–11.4
Galindo et al. [43]		EGR	Gas	2.6	0	3.9
Reihani et al. [42]		EGR	Gas	11.2	0	0.2–7
Galindo et al. [35]		EGR	Gas	5	35	0.1–1.1
Hirota et al. [69]		Cooling	Gas	2	0	0.2–3.4
Kimura et al. [2]		Nuclear	Water	9	0	0.5–19
Bo Su et al. [70]		Nuclear	Water	10.2	0	20.4
Evrim et al. [12]		Nuclear	Water	3.4	0	0.01

Kamide et al. [10] employed main-to-branch momentum ratio M_R to establish the boundaries between flow modes. By virtue of Eq. 21

$$J = \frac{4 \cdot D_m}{\pi \cdot D_b} \cdot \frac{1}{M_R}, \tag{21}$$

the thresholds of Kamide et al. [10] can be translated in terms of J. In this way, $J < 2.037$ should present a wall-jet pattern, $J > 7.857$ is expected to feature an impinging jet and intermediate values of $2.037 < J < 7.857$ should behave as a deflected jet. Therefore, the numerical campaign conducted in this work spans over a wide range of momentum ratio J that include the flow modes of Kamide et al. [10], as indicated by Table 5.

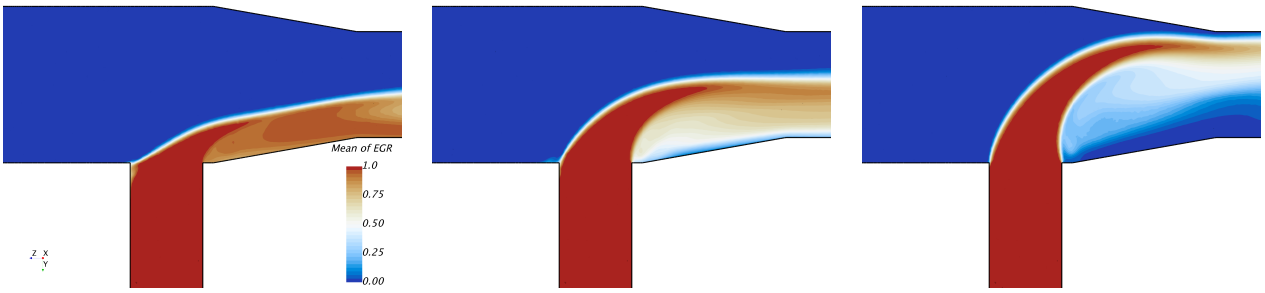

Figure 9: Time-averaged contours of passive scalar for wall-jet mode (left), deflecting-jet (middle) and impinging-jet (right).

To perform a fair comparison between flow patterns, 3 working points are studied in this section in which all the boundary conditions of Table 2 will be constant except for the EGR rate, which will subsequently determine the branch mass flow rate (see Eq. 6) as well as momentum ratio J (see Eq. 9). The exact values of EGR_{rate} and J for the working points representing the different flow patterns are included in Table 6.

Table 6: EGR_{rate} and J for the selected representatives of the flow patterns.

Jet pattern	Wall	Deflecting	Impinging
EGR_{rate}	0.1	0.25	0.4
J	1.27	2.86	11.42

Figure 9 depicts contours of passive scalar ϕ for the 3 working points aforementioned at the longitudinal plane of Fig. 1. Besides, Fig. 10 shows contours of mass fraction of condensed water Y_{H_2O-liq} (top row), passive scalar ϕ (middle row) and temperature (bottom row) for the same working points at the postprocessing cross-section displayed in Fig. 1. All these scalar fields have been time-averaged.

The analyzed flow patterns present significant differences. First, the wall-jet mode (on the left part of Fig. 9) presents a branch stream which does not have enough momentum to penetrate in the main stream, so that it is attached to the lower wall (see middle left part of Fig. 10). In this case, condensation is produced essentially at the interface between both streams (see top left part of Fig. 10), where temperature can get below dew conditions (see bottom left part of Fig. 10) and diffusive mixing should take place. To prove the latter, the time-averaged magnitude of the gradient of passive scalar ϕ, $\|\nabla\bar{\phi}(t)\|$, is compared against the condensed water in Fig. 11, showing the qualitative resemblance between these variables.

When the branch stream grows in momentum, it is able to enter into the main duct. For the deflecting-jet mode depicted on the middle of Fig. 9, the branch stream is not able to reach the top wall, being deflected by the inlet stream midway. In this case, the branch stream greater inertia prevents it from turning sharply into the lower wall, thus creating a flow detachment and a subsequent region of lower pressure. A fraction of the inlet stream is then encouraged to take this place by surrounding the branch stream. Now, the core of the branch stream is shifted upwards

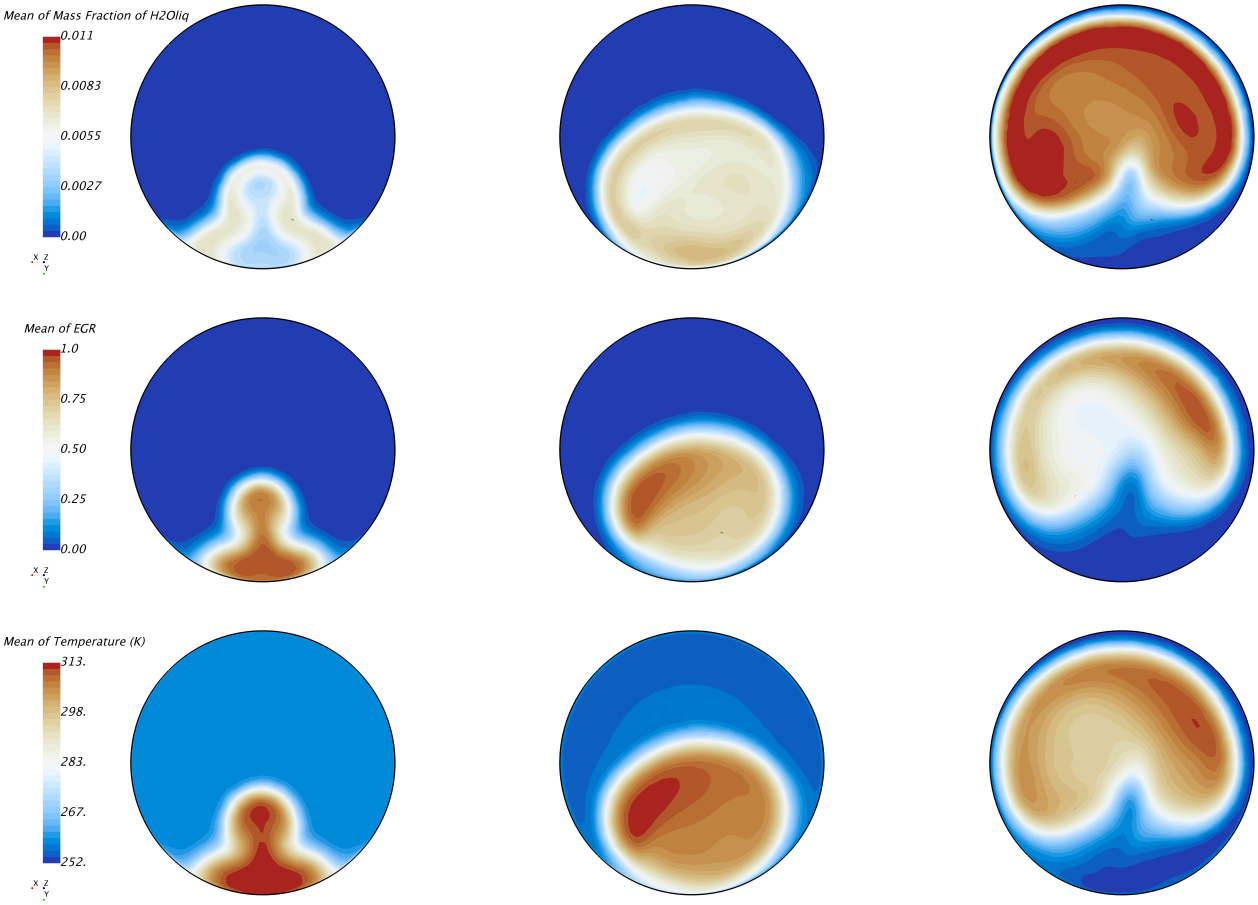

Figure 10: Time-averaged results of Y_{H_2O-liq} (top row), passive scalar (middle row) and temperature (bottom row) contours at postprocessing section (Figure 1), for wall-jet flow mode (left column), deflecting-jet (middle column) and impinging-jet (right column).

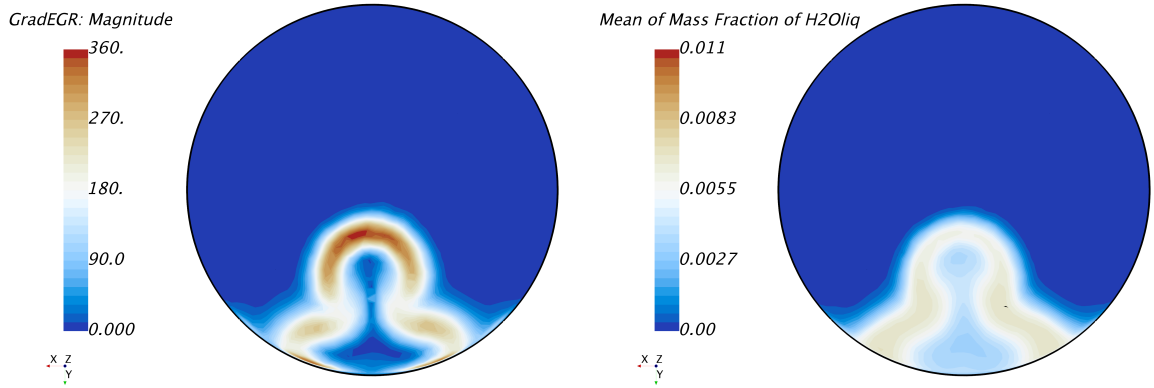

Figure 11: Time-averaged contours of $\|\nabla\bar{\phi}(t)\|$ (left) and Y_{H_2O-liq} (right) at postprocessing section (Figure 1), for wall-jet flow mode.

(see central element of Fig. 10) and is more diluted with the inlet stream, extending the locus of temperature below dew conditions (bottom middle part of Fig. 10) and thus expanding the region at which condensation appears (see top middle part of Fig. 10).

Finally, the branch stream may be fast enough to get close or hit the upper wall, which is known as impinging-jet pattern (right part of Fig. 9). The inlet stream is more prone to encircle the branch jet, so the regions for the inlet and branch streams are switched (see right middle part of Fig. 10). The enhanced mixing mechanisms promoted by the secondary flows due to impinging-jet pattern increases not only the extension of the condensing region but also its intensity (see top right part of Fig. 10), therefore boosting condensation.

3.4. Impact of momentum ratio (J) on mixing

Section 3.1 proposed a regression for condensation on the basis of psychrometry and mixing, through Eq. 18. Indeed, the comprehensive numerical campaign designed in Section 2.3 shifts all the factors considered in table 2 when moving across the different working points, which entails changes in both psychrometric conditions and mixing mechanisms. To provide a meaningful analysis useful for junction designers, it makes sense to consider that the psychrometric conditions cannot be modified. In the spirit of Eq. 18, this would imply that $\dot{m}_{cond-0D}$ is a given value, and a minimization of $\dot{m}_{cond}$ can only be obtained by means of decreasing the mixing index MI. In accordance with Section 2.1, it can be estimated how modifying the factors involved in $\dot{m}_{cond-0D}$ ($\dot{m}_m$, EGR_{rate}, T_m, T_b, RH_m, w_b and P_{outlet}) result in a change in condensation, through psychrometry. However, the absence of an analytical model for mixing (which should be based on the information of table 2 and the junction geometry) makes it more challenging to determine the impact of these features on mixing, although Section 3.2 has already provided some guidelines to reduce mixing and condensation by considering a single operating condition. To understand the influence of the change in working point on mixing, condensation is omitted in this section and the analysis is focused only on MI, seeking the key parameter related to the boundary conditions that determines how well mixed are both streams at the target cross-section. In light of the mixing flow patterns described in Section 3.3, this section is devoted to the quantification of the correlation between mixing indexes MI and momentum ratio J.

The same 128 simulations considered in Section 3.1 are now employed to perform a linear regression between the mixing indexes defined in Section 2.5 and the branch-to-main momentum ratio J (Eq. 8). The R^2 coefficients (see Eq. 20) for these regressions are presented in Table 7:

Table 7: Coefficient of determination (R^2) for linear regressions of mixing indexes vs momentum ratio J

Mixing index	R^2
$MI_{\phi-new}$	0.97
$MI_{\phi-ref}$	0.67
MI_{T-new}	0.89
MI_{T-ref}	0.67

Table 7 shows that mixing can be quantified to a high degree just by considering momentum ratio J for the new mixing indexes proposed in this work. However, the linear regression for the reference indexes is much weaker. To gain more insight into the impact of momentum ratio on mixing, Fig. 12 presents a scatter plot considering $MI_{\phi-new}$ (Eq. 11) and $MI_{\phi-ref}$ (Eq. 10) against J for the 128 simulations.

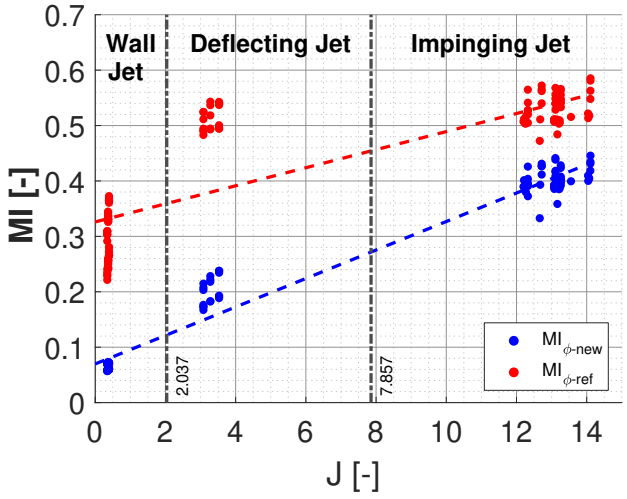

Figure 12: Scatter plot of mixing indexes at postprocessing section (Fig. 1) versus momentum ratio J for the 128 simulations of the numerical campaign, with linear regressions and regions of different flow patterns.

Figure 12 shows that the numerical campaign presents J values grouped around 0.35, 3.5 and 13; which are determined essentially by the EGR rates of Table 2. Figure 12 also includes the thresholds calculated with Eq. 21, confirming that all 3 flow patterns are represented within the numerical campaign. Figure 12 displays greater values of $MI_{\phi-ref}$ compared to $MI_{\phi-new}$ for all momentum ratios J. Considering Eq. 18, a greater value of MI provides a higher value of $\dot{m}_{cond-pred}$, which will improve the agreement with $\dot{m}_{cond-obs}$ considering the underprediction found for all types of MI in Figs. 4 and 5. Therefore, the greater values of $MI_{\phi-ref}$ against $MI_{\phi-new}$ result in the lower MAE of the former technique (see Table 3). In any case, both trend lines depicted in Fig. 12 show an increase of mixing with J as suggested by Section 3.3, but there is an important difference of performance between mixing indexes.

Table 7 presented a much better goodness of fit between J and $MI_{\phi-new}$ ($R^2 = 0.97$) than the one existing between J and $MI_{\phi-ref}$ ($R^2 = 0.67$). This is confirmed by Fig. 12, in which the values of $MI_{\phi-new}$ do not depart significantly from their regression line. $MI_{\phi-ref}$ instead provides similar values for deflecting and impinging jet situations, whereas cases with wall jet pattern present lower $MI_{\phi-ref}$ values but with a great dispersion. This may seem contradictory to the high $R^2 = 0.95$ (see Table 4) found for the linear regression of $MI_{\phi-ref} \cdot \dot{m}_{cond-0D}$. However, the close up of Fig. 4 reveals points with huge dispersion at $\dot{m}_{cond}$ close to zero and overpredicted points at $\dot{m}_{cond} \simeq 0.1 kg/s$. The poor performance of $MI_{\phi-ref}$ displayed in Fig. 12 does not affect though the impinging jet working points, which present highest J. These cases are obtained with greatest EGR_{rate} (see Eq. 9) and $\dot{m}_b$ (see Eq. 6), so provide more condensation, as the branch stream is the one with high humidity.

3.5. Reducing mixing and condensation by decreasing momentum ratio

Section 3.4 has shown that there is a positive correlation between mixing and J, whereas section 3.1 proved that greater condensation occurs for higher values of MI. Therefore, this section is devoted to the reduction of mixing and condensation by lowering momentum ratio J.

Assuming perfect gas behavior and neglecting the difference in pressure drop between junction legs[2] and the impact of humidity on density, Eq. 9 is simplified as

$$J = \frac{EGR_{rate}{}^2 \cdot T_b \cdot A_m^2}{(1 - EGR_{rate})^2 \cdot T_m \cdot A_b^2} \cdot cos(\alpha) \, , \tag{22}$$

which depends on boundary conditions of Table 2 and junction design parameters (A_m, A_b, α). Therefore, for a given working point, Eq. 22 implies that J can be reduced by lowering A_m or increasing A_b and α (see Fig. 1). In this section, the main duct area (A_m) is not modified, as reducing it may contravene other design constraints in terms of pressure drop.

A baseline case with the same A_b and $\alpha = 0°$ as the original junction depicted in Fig. 1 is considered. The selected operating conditions correspond to the impinging-jet mode of section 3.3, so that there is room to obtain lower values of J. This is the same point shown in the psychrometric chart of Fig. 2 and also employed in section 3.2. The axis of the branch duct is moved upstream 0.5 diameters, to allow the possibility of implementing the upcoming geometrical modifications. The impact of varying either the area of the branch (A_b) or the branch insertion angle (α) on J, $MI_{\phi-new}$ and condensation is assessed with the following 4 additional cases:

- 2 cases with $2 \cdot A_b$ and $4 \cdot A_b$.
- 2 cases with $\alpha = 30°$ and $\alpha = 60°$

Figure 13 presents the results at the postprocessing section (see Fig. 1) for the aforementioned cases in terms of $MI_{\phi-new}$ (left vertical axis) and generated condensation $\dot{m}_{cond}$ (right vertical axis). In these parametric analyses the variable not assessed is kept at its default value (A_b or $\alpha = 60°$), so the red labels of Fig. 13 indicate only the modified parameter. Figure 13 confirms that increasing branch duct area A_b and angle α reduces J and, in turn, condensation and mixing. The considered working point presents an impinging jet mode with the baseline geometry. With the proposed modifications in A_b and α, the same working point could exhibit a deflected jet or even a wall jet pattern, correspondingly.

Figure 13 shows that the sensitivity of $\dot{m}_{cond}$ and $MI_{\phi-new}$ to J is greater when increasing than α when enlarging A_b. To provide some insight into this characteristic, contours of ϕ are depicted in Fig. 14 for junction simulations featuring $\alpha = 60°$ and $4 \cdot A_b$. These two cases present similar values for condensation and mixing according to Fig. 13, despite their great difference in terms of J. Indeed, top part of Fig. 14 shows that the junction with $\alpha = 60°$ behaves

[2] $\frac{p_m}{p_b}$ is comprised between 1 and 1.02 for the whole numerical campaign.

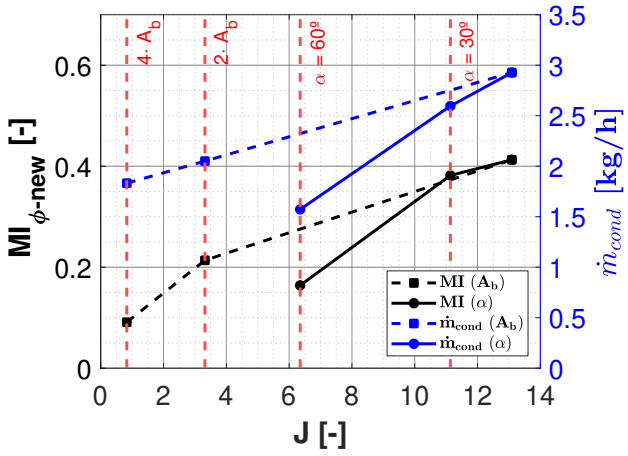

Figure 13: Time-averaged results of $MI_{\phi-new}$ and $\dot{m}_{cond}$ at postprocessing section (Fig. 1) versus momentum ratio J, when modifying branch duct area A_b and angle α.

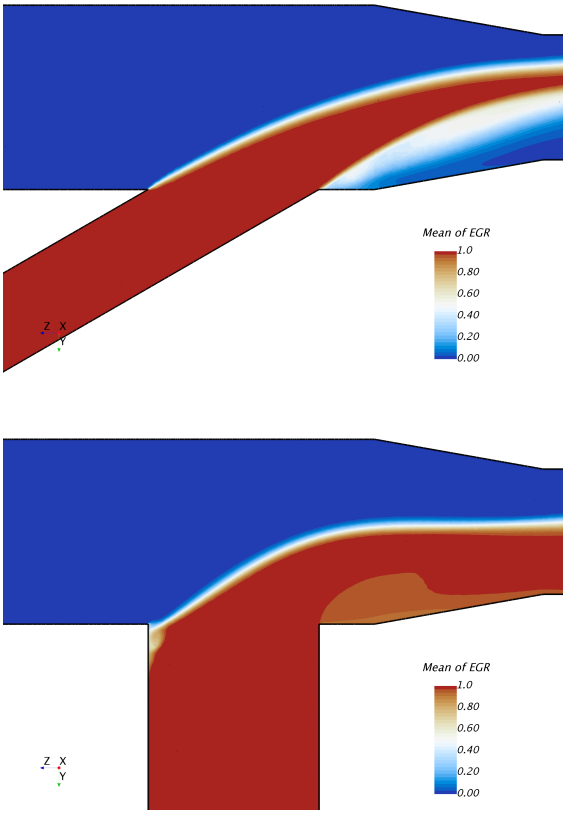

Figure 14: Time-averaged contours of passive scalar at longitudinal postprocessing section (Figure 1), for cases with $\alpha = 60°$ (top) and $4 \cdot A_b$ (bottom).

as a deflecting jet, whereas bottom part of Fig. 14 displays a wall jet pattern for the case with $4 \cdot A_b$. However, the flow field of the junction with $\alpha = 60°$ differs from the deflecting jet shown in middle part of Fig. 9. In the latter, the branch leg is perpendicular to the inlet and outlet ducts. The stream injected by the branch at middle of Fig. 9 is therefore dragged by the inlet flow, creating a wake downstream the jet that enhances mixing. Instead, the junction with $\alpha = 60°$ discharges the branch stream with momentum in direction of the outlet duct, so the wake region and the subsequent boost in mixing is greatly reduced (see top part of Fig. 14). Besides, the lower branch cross section compared to the case $4 \cdot A_b$ provides a higher velocity for the jet, which entails a lower residence time for the branch stream to mix with the inlet one.

4. Concluding remarks

In this work, a fractional factorial design of a numerical campaign consisting of 128 RANS/URANS simulation of two humid streams merging in a T-junction has been conducted. These simulations have been employed to analyze the correlation between flow mixing and volume condensation. To do so, a method to define new mixing indexes through the calculation of the unmixed area has been developed. In this work, the mixing indexes have been computed on the basis of a passive scalar and temperature, considering a linear weighting to determine the fraction of unmixed area provided by each grid element.

Condensation mass flow rate has been found to correlate linearly with high coefficients of determination for all mixing indexes, when psychrometric conditions are taken into account throughout a 0D perfect mixing model. For a given working point, the psychrometric conditions are fixed, so the junction designers should focus on reducing mixing if a decrease of bulk condensation is sought. The usage of a passive scalar will allow simulation engineers to optimize junction geometries in terms of mixing and condensation without requiring to consider an in-flow condensation submodel, such as the one employed in this work. Likewise, a humid flow test bench is not needed to assess the behavior of a junction in terms of potential condensation generation, as temperature measurements will suffice. However, both numerical and experimental researchers cannot circumvent these elements (condensation submodel or humid test bench, respectively) if the quantification of the condensation mass flow rate is required. The correlation proposed consistently underpredicts condensation and can be used as a surrogate model only after being calibrated. Conducting similar numerical campaigns with additional junction geometries could be useful to determine whether other weightings for the new mixing indexes provide better *a priori* agreement to predict condensation mass flow rate than the linear weighting employed in this work.

This work also provides a set of universal guidelines to design junctions with reduced volume condensation, as they have shown to achieve this through the decrease of flow mixing. In this way, valves employed to adjust operating conditions should be placed in other elements or as far as possible from the intersection of ducts. This intersection in turn should be located as close as possible from the target location at which condensation should be minimized. Besides, the branch-to-main momentum ratio J has been found to be a key factor governing the flow patterns and

therefore the mixing of inlet streams. Designing a branch leg aligned towards the outlet duct with a diameter as large as possible is likely to provide a wall-jet mode that greatly reduces mixing and condensation. If junction geometry is optimized and impinging-jet flow patterns are avoided in favor of wall-jet and deflecting-jet modes, the new mixing indexes have been found to perform better than the ones considered as references by the literature.

5. Acknowledgements

The authors of this paper wish to thank Andrea Conchado for helping with the fractional factorial design of the numerical campaign and Francisco Moya for his support with the 0D condensation model. This work has been partially supported by Conselleria de Innovación, Universidades, Ciencia y Sociedad Digital de la Generalitat Valenciana through grant number GV/2020/008.

References

[1] J. Kickhofel, V. Valori, H.-M. Prasser, Turbulent penetration in t-junction branch lines with leakage flow, Nuclear Engineering and Design 276 (2014) 43–53. doi:10.1016/j.nucengdes.2014.05.002.

[2] N. Kimura, H. Ogawa, H. Kamide, Experimental study on fluid mixing phenomena in t-pipe junction with upstream elbow, Nuclear Engineering and Design 240 (10) (2010) 3055–3066. doi:10.1016/j.nucengdes.2010.05.019.

[3] T. Lu, D. Attinger, S. M. Liu, Large-eddy simulations of velocity and temperature fluctuations in hot and cold fluids mixing in a tee junction with an upstream straicht or elbow main pipe, Nuclear Engineering and Design 263 (2013) 32–41. doi:10.1016/j.nucengdes.2013.04.002.

[4] J. Galindo, H. Climent, R. Navarro, G. García-Olivas, Assessment of the numerical and experimental methodology to predict egr cylinder-to-cylinder dispersion and pollutant emissions, International Journal of Engine Research 22 (10) (2021) 3128–3146. doi:10.1177/1468087420972544.

[5] J. Galindo, R. Navarro, D. Tarí, G. García-Olivas, Centrifugal compressor influence on condensation due to Long Route-Exhaust Gas Recirculation mixing, Applied Thermal Engineering 144 (2018) 901 – 909. doi:10.1016/j.applthermaleng.2018.09.005.

[6] L. Yang, J. Wang, Y. Jiang, L. Zou, Oil-water flow splitting in eccentric annular t-junction tubes. experimental and cfd analysis, Chemical Engineering Science 228 (2020) 116000. doi:10.1016/j.ces.2020.116000.

[7] S. M. Hosseini, K. Yuki, H. Hashizume, Classification of turbulent jets in a t-junction area with a 90-deg bend upstream, International Journal of heat and mass transfer 51 (9-10) (2008) 2444–2454. doi:10.1016/j.ijheatmasstransfer.2007.08.024.

[8] X. Li, S. Wang, Flow field and pressure loss analysis of junction and its structure optimization of aircraft hydraulic pipe system, Chinese Journal of Aeronautics 26 (4) (2013) 1080–1092. doi:10.1016/j.cja.2013.04.004.

[9] M. Zhou, R. Kulenovic, E. Laurien, T-junction experiments to investigate thermal-mixing pipe flow with combined measurement techniques, Applied Thermal Engineering 150 (2019) 237–249. doi:10.1016/j.applthermaleng.2018.12.161.

[10] H. Kamide, M. Igarashi, S. Kawashima, N. Kimura, K. Hayashi, Study on mixing behavior in a tee piping and numerical analyses for evaluation of thermal striping, Nuclear Engineering and Design 239 (1) (2009) 58–67. doi:10.1016/j.nucengdes.2008.09.005.

[11] C. Evrim, X. Chu, E. Laurien, Analysis of thermal mixing characteristics in different t-junction configurations, International Journal of Heat and Mass Transfer 158 (2020) 120019. doi:10.1016/j.ijheatmasstransfer.2020.120019.

[12] C. Evrim, E. Laurien, Numerical study of thermal mixing mechanisms in t-junctions, Applied Thermal Engineering 183 (2021) 116155. doi:10.1016/j.applthermaleng.2020.116155.

List of Symbols

A	area	m^2
dA	differential area	m^2
α	branch insertion angle	$^\circ$
D	duct diameter	m
ϵ	local mixing rate	–
f_v	viscous forces	$kg \cdot m \cdot s^{-2}$
I	turbulent intensity	$\%$
J	normal branch-to-main momentum ratio	–
K	total number of simulations inside the numerical campaign	–
L	latent heat	$J \cdot kg^{-1}$
$\dot{m}$	mass flow rate	$kg \cdot s^{-1}$
MI	mixing index	–
M_R	main-to-branch momentum ratio	–
N	number of elements in a cross-section	–
P	pressure	Pa
R^2	correlation coefficient	–
ϕ	scalar composition	–
RH	relative humidity	$\%$
S	source term	
T	temperature	K
U	velocity magnitude	$m \cdot s^{-1}$
$\vec{u}$	velocity	$m \cdot s^{-1}$
w	specific humidity	$g_{H_2O} \cdot kg_{air}^{-1}$
w_v	viscous work	$kg \cdot m^{-1} \cdot s^{-3}$
Y	mass fraction	–
Δt	time-step size	s
ρ	density	$kg \cdot m^{-3}$

[13] A. Kuczaj, E. Komen, M. Loginov, Large-Eddy Simulation study of turbulent mixing in a T-junction, Nuclear Engineering and Design 240 (9) (2010) 2116 – 2122, experiments and CFD Code Applications to Nuclear Reactor Safety (XCFD4NRS). doi:10.1016/j.nucengdes.2009.11.027.

[14] A. Gupta, M. S. Ibrahim, R. Amano, Effect of jet-to-mainstream momentum flux ratio on mixing process, Heat and Mass Transfer 52 (3) (2016) 621–634. doi:10.1007/s00231-015-1582-7.

[15] I. Basler, H. Reister, R. Rossmann, B. Weigand, A simulation method for the calculation of water condensation inside charge air coolers (2021). doi:10.4271/2021-01-0226.

Sub- and Superscripts

0	stagnation variable
ad	adiabatic
adim	non-dimensional
b	branch
i	certain cell face
k	certain simulation inside the numerical campaign
m	main
norm	normalized
PM	perfect mixing
ref	reference value
sat	saturation

List of abbreviations and acronyms

0D	zero dimensional
3D	three dimensional
CFD	computational fluid dynamics
EGR	exhaust gas recirculation
LIC	line integral convolution
LP-EGR	low pressure EGR
M	millions of cells
NOx	nitrogen oxides
RANS	Reynolds-averaged Navier-Stokes

[16] R. Cash, A. Talekar, B. AbdulNour, A cfd study of water condensation inside the tubes of an automotive compact charge air cooler using large eddy simulation approach, in: ASME International Mechanical Engineering Congress and Exposition, Vol. 50626, American Society of Mechanical Engineers, 2016, p. V008T10A068. doi:10.1115/imece2016-66999.

[17] K. R. Jensen, P. Fojan, R. L. Jensen, L. Gurevich, Water condensation: A multiscale phenomenon, Journal of nanoscience and nanotechnology 14 (2) (2014) 1859–1871. doi:10.1166/jnn.2014.9108.

[18] Q. Sheng, J. Sun, Q. Wang, W. Wang, H. S. Wang, On the onset of surface condensation: formation and transition mechanisms of condensation mode, Scientific reports 6 (1) (2016) 1–9. doi:10.1038/srep30764.

[19] N. Kortsenshtein, E. Samuilov, A. Yastrebov, New method of simulation of volume condensation of supersaturated vapor, High Temperature 47 (1) (2009) 83–94. doi:10.1134/s0018151x09010118.

[20] P. Vojkuvkova, O. Sikula, J. Weyr, Assessment of condensation of water vapor in the mixing chamber by CFD method, in: EPJ Web of Conferences, Vol. 92. doi:10.1051/epjconf/20159202112.

[21] J. R. Serrano, P. Piqueras, E. Angiolini, C. Meano, J. De La Morena, On cooler and mixing condensation phenomena in the long-route exhaust gas recirculation line, in: SAE Technical Paper, 2015. doi:10.4271/2015-24-2521.

[22] M. Zheng, G. T. Reader, J. G. Hawley, Diesel engine exhaust gas recirculation—-a review on advanced and novel concepts, Energy conversion and management 45 (6) (2004) 883–900.

[23] Y. Park, C. Bae, Experimental study on the effects of high/low pressure egr proportion in a passenger car diesel engine, Applied energy 133 (2014) 308–316. doi:10.1016/j.apenergy.2014.08.003.

[24] M. Choi, K. Mohiuddin, N. Kim, S. Park, Investigation of the effects of egr rate, injection strategy and nozzle specification on engine performances and emissions of a single cylinder heavy duty diesel engine using the two color method, Applied Thermal Engineering (2021) 117036doi:10.1016/j.applthermaleng.2021.117036.

[25] J. M. Desantes, J. M. Luján, B. Pla, J. A. Soler, On the combination of high-pressure and low-pressure exhaust gas recirculation loops for improved fuel economy and reduced emissions in high-speed direct-injection engines, International Journal of Engine Research 14 (1) (2013) 3–11. doi:10.1177/1468087412437623.

[26] J. M. Luján, C. Guardiola, B. Pla, A. Reig, Switching strategy between HP (high pressure)-and LPEGR (low pressure exhaust gas recirculation) systems for reduced fuel consumption and emissions, Energy 90 (2015) 1790–1798. doi:10.1016/j.energy.2015.06.138.

[27] A. García, J. Monsalve-Serrano, R. L. Sari, P. Gaillard, Assessment of a complete truck operating under dual-mode dual-fuel combustion in real life applications: Performance and emissions analysis, Applied Energy 279 (2020) 115729. doi:10.1016/j.apenergy.2020.115729.

[28] N. Dimitrakopoulos, G. Belgiorno, M. Tunér, P. Tunestål, G. Di Blasio, Effect of egr routing on efficiency and emissions of a ppc engine, Applied Thermal Engineering 152 (2019) 742–750. doi:10.1016/j.applthermaleng.2019.02.108.

[29] X. Yu, N. S. Sandhu, Z. Yang, M. Zheng, Suitability of energy sources for automotive application–a review, Applied Energy 271 (2020) 115169. doi:10.1016/j.apenergy.2020.115169.

[30] S. Karstadt, J. Werner, S. Münz, R. Aymanns, Effect of water droplets caused by low pressure EGR on spinning compressor wheels, in: Aufladetechnische Konferenz, Dresden, 2014.

[31] P. Olmeda, J. Martín, F. Arnau, S. Artham, Analysis of the energy balance during World harmonized Light vehicles Test Cycle in warmed and cold conditions using a Virtual Engine, International Journal of Engine Research - (2020) 0–18. doi:10.1177/1468087419878593.

[32] J. Galindo, R. Navarro, D. Tari, F. Moya, Development of an experimental test bench and a psychrometric model for assessing condensation on a Low Pressure EGR cooler, International Journal of Engine Research 22 (2020) 1540–1550. doi:10.1177/1468087420909735.

[33] H. Song, S. Song, Numerical investigation on a dual loop EGR optimization of a light duty diesel engine based on water condensation analysis 182 (2021) 1–12. doi:10.1016/j.applthermaleng.2020.116064.

[34] J. Serrano, P. Piqueras, R. Navarro, D. Tarí, C. Meano, Development and verification of an in-flow water condensation model for 3D-CFD simulations of humid air streams mixing, Computers & Fluids 167 (2018) 158 – 165. doi:10.1016/j.compfluid.2018.02.032.

[35] J. Galindo, R. Navarro, D. Tari, F. Moya, Analysis of condensation and secondary flows at T-junctions using optical visualization techniques and Computational Fluid Dynamics, International Journal of Multiphase Flow (2021). doi:10.1016/j.ijmultiphaseflow.2021.103674.

[36] J. Galindo, R. Navarro, D. Tarí, F. Moya, Quantitative validation of an in-flow water condensation model for 3D-CFD simulations of three-way junctions using indirect condensation measurements, International Journal of Thermal Sciences (2021). doi:10.1016/j.ijthermalsci.2021.107303.

[37] J. Galindo, P. Piqueras, R. Navarro, D. Tarí, C. Meano, Validation and sensitivity analysis of an in-flow water condensation model for 3D-CFD simulations of humid air streams mixing, International Journal of Thermal Sciences 136 (2019) 410 – 419. doi:10.1016/j.ijthermalsci.2018.10.043.

[38] K.-H. Brune, B. Stoffel, B. Matyschok, et al., Cfd-analysis of the flow consisting of two mass flows with different temperatures and/or two phases in a turbocompressor, in: ASME 2006 2nd Joint US-European Fluids Engineering Summer Meeting Collocated With the 14th International Conference on Nuclear Engineering, American Society of Mechanical Engineers Digital Collection, 2006, pp. 701–711.

[39] K.-H. Brune, H.-P. Schiffer, R. Christmann, M. Gnewikow, Experimental investigations of the disturbed inlet-flow structure caused by mixing geometries and its influence on the performance of a turbocharger centrifugal compressor, in: ASME Turbo Expo 2009: Power for Land, Sea, and Air, American Society of Mechanical Engineers Digital Collection, 2009, pp. 1295–1304.

[40] V. T. Vithala, J. Hoard, D. Assanis, D. Styles, 3-d numerical study of turbulent mixing of intake air and exhaust gas in a low pressure egr system, in: ASME 2011 Internal Combustion Engine Division Fall Technical Conference, American Society of Mechanical Engineers Digital Collection, 2011, pp. 893–904.

[41] A. Reihani, J. Hoard, S. Klinkert, C.-K. Kuan, D. Styles, Numerical evaluation of the effects of low pressure egr mixer configuration on turbocharger compressor performance, in: ASME 2018 Internal Combustion Engine Division Fall Technical Conference, American Society of Mechanical Engineers Digital Collection, 2018.

[42] A. Reihani, J. Hoard, S. Klinkert, C.-K. Kuan, D. Styles, G. McConville, Experimental response surface study of the effects of low-pressure exhaust gas recirculation mixing on turbocharger compressor performance, Applied Energy 261 (2020) 114349. doi:10.1016/j.apenergy.2019.114349.

[43] Galindo, J. and Serrano, J.R. and Navarro, R. and García Olivas, G., Numerical modeling of centrifugal compressors with heterogeneous incoming flow due to low pressure exhaust gas recirculation, in: Proceedings of ASME Turbo Expo 2020: Turbomachinery Technical Conference and Exposition, no. GT2020-16030, American Society of Mechanical Engineers, 2020. doi:10.1115/gt2020-16030.

[44] A. Sakowitz, M. Mihaescu, L. Fuchs, Turbulent flow mechanisms in mixing T-junctions by Large Eddy Simulations, International Journal of Heat and Fluid Flow 45 (2014) 135–146. doi:10.1016/j.ijheatfluidflow.2013.06.014.

[45] CD-adapco, STAR-CCM+, release version 12.06.010 Edition (February 2018).
URL http://ww.cd-adapco.com

[46] S. Schuster, D. Brillert, F. Benra, Condensation in Radial Turbines-Part I: Mathematical Modeling 140 1–9. doi:10.1115/1.4040934.

[47] S. Schuster, D. Brillert, F. Benra, Condensation in Radial Turbines-Part II: Application of the Mathematical Model to a Radial Turbine Series 140 1–7. doi:10.1115/1.4040935.

[48] T. Wittmann, C. Bode, J. Friedrichs, The Feasibility of an Euler-Lagrange Approach for the Modeling of Wet Steam 143 1–8. doi:10.1115/1.4049859.

[49] F. R. Menter, Two-equation eddy-viscosity turbulence models for engineering applications, AIAA journal 32 (8) (1994) 1598–1605. doi:10.2514/3.12149.

[50] S. Smith, M. Mungal, Mixing, structure and scaling of the jet in crossflow, Journal of fluid mechanics 357 (1998) 83–122. doi:10.1017/s0022112097007891.

[51] A. R. Karagozian, The jet in crossflow, Physics of Fluids 26 (10) (2014) 1–47. doi:10.1063/1.4895900.

[52] W. Vicente, M. Salinas-Vazquez, C. Chavez, E. Carrizosa, Different numerical methods in the study of passive scalar transport in a pipeline x-junction, Applied mathematical modelling 33 (3) (2009) 1248–1258. doi:10.1016/j.apm.2008.01.022.

[53] L. Grbčić, L. Kranjčević, I. Lučin, Z. Čarija, Experimental and numerical investigation of mixing phenomena in double-tee junctions, Water 11 (6) (2019) 1198. doi:10.3390/w11061198.

[54] A. Schlegel, M. Streichsbier, R. Mongia, R. Dibble, A Comparison of the Influence of Fuel/Air Unmixedness on NOx Emissions in Lean Premixed, Non-Catalytic and Catalytically Stabilized Combustion, Vol. 78699, American Society of Mechanical Engineers, 1997. doi:10.1115/97-gt-306.

[55] D. Mira, O. Lehmkuhl, P. Stathopoulos, T. Tanneberger, T. Reichel, C. Paschereit, M. Vázquez, G. Houzeaux, Numerical investigation of a lean premixed swirl-stabilized hydrogen combustor and operational conditions close to flashback, in: Turbo Expo: Power for Land, Sea, and Air, Vol. 51067, American Society of Mechanical Engineers, 2018, p. V04BT04A009. doi:10.1115/gt2018-76229.

[56] S. Hossain, M. Ansari, K.-Y. Kim, Evaluation of the mixing performance of three passive micromixers, Chemical Engineering Journal 150 (2-3) (2009) 492–501. doi:10.1016/j.cej.2009.02.033.

[57] P. Danckwerts, The definition and measurement of some characteristics of mixtures, Applied Scientific Research, Section A 3 (4) (1952) 279–296. doi:10.1016/b978-0-08-026250-5.50050-2.

[58] J. Andersen, F. Lindström, F. Westin, Surge definitions for radial compressors in automotive turbochargers, SAE International Journal of Engines 1 (1) (2008) 218–231. doi:10.4271/2008-01-0296.

[59] R. Dehner, N. Figurella, A. Selamet, P. Keller, M. Becker, K. Tallio, K. Miazgowicz, R. Wade, Instabilities at the low-flow range of a

turbocharger compressor, SAE International Journal of Engines 6 (2) (2013) 1356–1367. doi:10.4271/2013-01-1886.

[60] A. Torregrosa, A. Broatch, X. Margot, J. García-Tíscar, Y. Narvekar, R. Cheung, Local flow measurements in a turbocharger compressor inlet, Experimental Thermal and Fluid Science 88 (2017) 542 – 553. doi:10.1016/j.expthermflusci.2017.07.007.

[61] B. Smith, J. Mahaffy, K. Angele, A CFD benchmarking exercise based on flow mixing in a T-junction, Nuclear Engineering and Design 264 (2013) 80 – 88, sI:NURETH-14. doi:10.1016/j.nucengdes.2013.02.030.

[62] P. Slavík, B. Skočilasová, J. Soukup, F. Klimenda, Low pressure egr valve testing, in: AIP Conference Proceedings, Vol. 2118, AIP Publishing LLC, 2019, p. 030040. doi:10.1063/1.5114768.

[63] F. Castillo, E. Witrant, V. Talon, L. Dugard, Simultaneous air fraction and low-pressure egr mass flow rate estimation for diesel engines, IFAC Proceedings Volumes 46 (2) (2013) 731–736. doi:10.3182/20130204-3-fr-2033.00070.

[64] D. Wang, L. Shi, S. Zhu, B. Liu, Y. Qian, K. Deng, Numerical and thermodynamic study on effects of high and low pressure exhaust gas recirculation on turbocharged marine low-speed engine, Applied Energy 261 (2020) 114346. doi:10.1016/j.apenergy.2019.114346.

[65] G. Boccardo, F. Millo, A. Piano, L. Arnone, S. Manelli, C. Capiluppi, A fully physical correlation for low pressure egr control linearization, Tech. rep., SAE Technical Paper (2017). doi:10.4271/2017-24-0011.

[66] W. Wenzel, U. Hanig, J. Song, B. Bareis, M. Miclea-Bleiziffer, Inlet swirl throttle for passenger car engines, in: 16. Internationales Stuttgarter Symposium, Springer, 2016, pp. 951–968. doi:10.1007/978-3-658-13255-2_71.

[67] U. Hanig, M. Becker, Intake throttle and pre-swirl device for low-pressure egr systems, MTZ worldwide 76 (1) (2015) 10–13. doi:10.1007/s38313-014-1004-0.

[68] M. Hirota, E. Mohri, H. Asano, H. Goto, Experimental study on turbulent mixing process in cross-flow type t-junction, in: ICHMT DIGITAL LIBRARY ONLINE, Begel House Inc., 2009.

[69] M. Hirota, H. Asano, H. Nakayama, T. Asano, S. Hirayama, Three-dimensional structure of turbulent flow in mixing t-junction, JSME International Journal Series B Fluids and Thermal Engineering 49 (4) (2006) 1070–1077. doi:10.1299/jsmeb.49.1070.

[70] B. Su, Z. Zhu, X. Wang, H. Ke, M. Lin, Q. Wang, Effect of temperature difference on the thermal mixing phenomenon in a t-junction under inflow pulsation, Nuclear Engineering and Design 363 (2020) 110611. doi:10.1016/j.nucengdes.2020.110611.